Ocean Sci. Discuss., 9, 2915–2950, 2012
www.ocean-sci-discuss.net/9/2915/2012/
doi:10.5194/osd-9-2915-2012

Ocean Science Discussions

Fine-scale features on the sea surface in SAR satellite imagery – Part 2: Numerical modeling

S. Matt[1], A. Fujimura[2], A. Soloviev[1,2], S. H. Rhee[3], and R. Romeiser[2]

[1]Nova Southeastern University Oceanographic Center, Dania Beach, FL, USA
[2]University of Miami Rosenstiel School of Marine and Atmospheric Science, Miami, FL, USA
[3]Seoul National University, Department of Naval Architecture & Ocean Engineering, Seoul, Korea

Received: 30 June 2012 – Accepted: 12 August 2012 – Published: 17 September 2012

Correspondence to: S. Matt (silvia.matt@nova.edu, smatt@rsmas.miami.edu)

Published by Copernicus Publications on behalf of the European Geosciences Union.

Abstract

With the advent of the new generation of SAR satellites, it has become possible to resolve fine-scale features on the sea surface on the scale of meters. The proper identification of sea surface signatures in SAR imagery can be challenging, since some features may be due to atmospheric distortions (gravity waves, squall lines) or anthropogenic influences (slicks), and may not be related to dynamic processes in the upper ocean. In order to improve our understanding of the nature of fine-scale features on the sea surface and their signature in SAR, we have conducted high-resolution numerical simulations combining a three-dimensional non-hydrostatic computational fluid dynamics model with a radar imaging model. The surface velocity field from the hydrodynamic model is used as input to the radar imaging model. The combined approach reproduces the sea surface signatures in SAR of ship wakes, low density plumes, and internal waves in a stratified environment. The numerical results are consistent with observations reported in a companion paper of in-situ measurements during SAR satellite overpasses. Ocean surface and internal waves are also known to produce a measurable signal in the ocean magnetic field. This paper explores the use of computational fluid dynamics to investigate the magnetic signatures of oceanic processes. This potentially provides a link between SAR signatures of transient ocean dynamics and magnetic field fluctuations in the ocean. We suggest that combining SAR imagery with data from ocean magnetometers may be useful as an additional maritime sensing method. The new approach presented in this work can be extended to other dynamic processes in the upper ocean, including fronts and eddies, and can be a valuable tool for the interpretation of SAR images of the ocean surface.

1 Introduction

Synthetic aperture radar (SAR) imaging of the sea surface has long been recognized to be an important tool for ship surveillance, as well as oil spill and pollution monitoring.

OSD

9, 2915–2950, 2012

SAR satellite imagery may lead to information about dynamic processes in the upper ocean. Large amplitude internal waves are a well-documented example (Alpers, 1985; Hsu et al., 2000; Alpers et al., 2008; and others). Furthermore, under certain conditions, currents and winds can also be inferred from the new generation of SAR satellites (Horstmann et al., 2000; Romeiser et al., 2001, 2010; Brusch et al., 2008). However, atmospheric distortions and anthropogenic influences may complicate the interpretation of SAR satellite imagery (Alpers, 1985; Soloviev et al., 2012). Surfactants on the sea surface may also play an important role in the visibility of fine-scale features on the sea surface in SAR (Hühnerfuss et al., 1987; Gade et al., 1998; Soloviev et al., 2011; Matt et al., 2011).

Following the approach of Fujimura et al. (2012), we have combined a three-dimensional non-hydrostatic computational fluid dynamics (CFD) model with a radar imaging model to study the sea surface signatures in synthetic aperture radar (SAR) of fine-scale oceanic features. This computational approach is used here in application to ship wakes, low density plumes, and internal wave solitons.

In this work, a numerical model of centerline wakes of ships is employed to investigate the impact of stratification on the wake hydrodynamics. The hydrodynamics of far wakes of ships with application to SAR remote sensing have previously been studied by various authors (Milgram et al., 1993a, b; Reed and Milgram, 2002; Soloviev et al., 2008, 2010) and it is a topic which has important practical applications. Fujimura et al. (2010, 2012) found that wind stress across the ship wake leads to an asymmetry in the wake surface signature in the simulated radar image. Here, we use their model of the ship wake and extend the analysis to include an ambient thermal stratification.

The dynamics of low density plumes and their interaction with ambient near-surface stratification, as well as an internal wave soliton are also investigated. Buoyancy-driven surface currents, such as propagating river or rain-formed plumes, are an important component of the oceanic environment. These currents contribute to water mass exchange by horizontal advection and enhanced vertical mixing. These buoyancy-driven flows are a type of organized structure that resembles a classical gravity current.

OSD
9, 2915–2950, 2012

Fujimura et al. (2011) showed that as in the case of the ship wake, wind stress can lead to an asymmetry in the sea surface signatures of rain-formed low density plumes. Near-surface gravity currents may also interact with an ambient stratification in a resonant way, leading to a fragmentation of the near-surface plume (Soloviev and Lukas, 2006).

Ocean surface and internal waves have been reported to lead to a measureable signal in the ocean electromagnetic field (Crews and Futterman, 1962; Beal and Weaver, 1970). These magnetic field perturbations arise by induction, through the motion of the conducting sea water through the Earth's magnetic field. A better understanding of the magnetic fields induced by oceanographic processes is important for ship detection and other naval applications. As part of this work, the use of CFD to study the magnetic signatures of oceanic fine-scale processes is explored. We have been able to simulate electromagnetic signatures of internal waves, buoyancy driven currents associated with low density near-surface plumes, and ship wakes in the ocean magnetic field. Based on our results, we argue that combining SAR with data from ocean magnetometers has the potential to become a valuable additional maritime sensing method.

The paper is structured as follows. Section 2 describes the hydrodynamic and electromagnetic model, as well as the model setup and parameters. It briefly discusses the usage of the radar imaging model. In Sect. 3, the results from our numerical simulations are presented. Summary and discussion conclude the article in Sect. 4.

2 Methods

CFD models, by default, are non-hydrostatic and often three-dimensional and high-resolution numerical models that are routinely applied to engineering problems. Here, the CFD code ANSYS Fluent is used to study the dynamics of upper ocean fine-scale processes, which are inherently three-dimensional and non-hydrostatic. The model uses a control volume approach to solve conservation equations for mass and momentum. The following sections describe the model equations for both hydrodynamic

OSD
9, 2915–2950, 2012

and electromagnetic model, as well as the model setup and parameters. The detailed description of the M4S radar imaging model used in this study is beyond the scope of this paper and we provide only a brief overview of its usage.

2.1 Hydrodynamic model

Despite recent advances in computing power, it is still computationally prohibitive to numerically solve the fully three-dimensional Navier-Stokes equations for turbulent processes at all scales and for realistic domain sizes. In the so-called Large Eddy Simulation (LES) turbulence model, the assumption is that most of the energy is contained in the large eddies and overturns in the flow and hence the model aims to explicitly resolve the scales of these large eddies, while the subgrid scales are modeled. The governing equations for LES are obtained by filtering the time-dependent Navier-Stokes equations. The process filters out eddies with scales smaller than the filter width or grid spacing, and the resulting equations govern the dynamics of the large eddies (Sagaut, 1998).

The model solves the filtered Navier-Stokes equations, which are given as follows:

$$\frac{\partial \rho}{\partial t} + \frac{\partial}{\partial x_i}(\rho \bar{u}_i) = 0 \tag{1}$$

$$\frac{\partial}{\partial t}(\rho \bar{u}_i) + \frac{\partial}{\partial x_j}\left(\rho \bar{u}_i \bar{u}_j\right) = \frac{\partial}{\partial x_j}(\sigma_{ij}) - \frac{\partial \bar{p}}{\partial x_i} - \frac{\partial \tau_{ij}}{\partial x_j} \tag{2}$$

where σ_{ij} is the stress tensor due to molecular viscosity defined by

$$\sigma_{ij} = \left[\mu\left(\frac{\partial \bar{u}_i}{\partial x_j} + \frac{\partial \bar{u}_j}{\partial x_i}\right)\right] - \frac{2}{3}\mu \frac{\partial u_l}{\partial x_l}\delta_{ij} \tag{3}$$

and τ_{ij} is the subgrid-scale stress defined by

$$\tau_{ij} \equiv \rho\overline{u_i u_j} - \rho \bar{u}_i \bar{u}_j. \tag{4}$$

OSD
9, 2915–2950, 2012

The subgrid-scale stresses resulting from the filtering operation need to be modeled. Using the Boussinesq hypothesis (Hinze, 1975), the subgrid-scale stresses are computed from:

$$\tau_{ij} - \frac{1}{3}\tau_{kk}\delta_{ij} = -2\mu_t \bar{S}_{ij}, \tag{5}$$

where μ_t is the subgrid-scale turbulent viscosity. τ_{kk} is the isotropic part of the subgrid-scale stresses, which is not modeled but added to the term containing the static pressure in the filtered Navier-Stokes equations. The rate-of-strain tensor for the resolved scales is

$$\bar{S}_{ij} = \frac{1}{2}\left(\frac{\partial \bar{u}_i}{\partial x_j} + \frac{\partial \bar{u}_j}{\partial x_i}\right). \tag{6}$$

To calculate the turbulent viscosity μ_t, we apply the so-called Wall-Adapting Local Eddy-Viscosity (WALE) model (Nicoud and Ducros, 1999) for the simulation of the ship wake and low density buoyant plume in the near-surface layer of the ocean. The WALE model improves the LES performance near a solid boundary. For the simulation of an internal wave in the thermocline, the traditional Smagorinsky-Lilly model is used (Smagorinksy, 1963).

In the WALE model, the eddy viscosity becomes

$$\mu_t = \rho L_s^2 \frac{\left(S_{ij}^d S_{ij}^d\right)^{3/2}}{\left(\bar{S}_{ij}\bar{S}_{ij}\right)^{5/2} + \left(S_{ij}^d S_{ij}^d\right)^{5/4}}, \tag{7}$$

and L_s and S_{ij}^d are defined as follows

$$L_s = \min(\kappa d, C_w \Delta) \tag{8}$$

OSD
9, 2915–2950, 2012

$$S_{ij}^{d} = \frac{1}{2}\left(\bar{g}_{ij}^{2} + \bar{g}_{ji}^{2}\right) - \frac{1}{3}\delta_{ij}\bar{g}_{kk}^{2}, \bar{g}_{ij} = \frac{\partial \bar{u}_i}{\partial x_j}. \quad (9)$$

Here, $L_s$is the mixing length for the subgrid scales, κ is the von Kármán constant, d is the distance closest to the wall and V is the volume of the computational cell and the local grid scale $\Delta = V^{1/3}$. C_w is a constant and set to the default value of $C_w = 0.325$.

In the Smagorinsky-Lilly model, μ_t is computed from

$$\mu_t = \rho L_s^2 \sqrt{2\bar{S}_{ij}\bar{S}_{ij}}, \quad (10)$$

where

$$L_s = \min(\kappa d, C_s \Delta) \quad (11)$$

and C_s is a constant with $C_s = 0.1$.

The filtered energy equation is

$$\frac{\partial \rho \bar{h}_s}{\partial t} + \frac{\partial \rho \bar{u}_i \bar{h}_s}{\partial x_i} - \frac{\partial \bar{p}}{\partial t} - \bar{u}_j \frac{\partial \bar{p}}{\partial x_i} - \frac{\partial}{\partial x_i}\left(\lambda \frac{\partial \bar{T}}{\partial x_i}\right) = -\frac{\partial}{\partial x_j}\left[\rho\left(\overline{u_i h_s} - \bar{u}_i \bar{h}_s\right)\right] \quad (12)$$

Here, h_s and λ are the sensible enthalpy and the thermal conductivity, respectively.

The term in angular brackets on the right-hand side of Eq. (12) is the subgrid enthalpy flux and is approximated by

$$\rho\left(\overline{u_i h_s} - \bar{u}_i \bar{h}_s\right) = -\frac{\mu_t C_p}{\sigma_t}\frac{\partial \bar{T}}{\partial x_j}, \quad (13)$$

where σ_t is the subgrid-scale turbulent Prandtl number, $\sigma_t = 0.85$.

Finally, the subgrid-scale turbulent flux q_j of a scalar Φ is calculated from

$$q_j = -\frac{\mu_t}{\sigma_t}\frac{\partial \Phi}{\partial x_j}. \quad (14)$$

OSD
9, 2915–2950, 2012

2.2 Electromagnetic model

The equations governing a magnetic field are the Maxwell equations (Crews and Futterman, 1962).

$$\nabla \times \frac{\boldsymbol{B}}{\mu_{\mathrm{m}}} = \boldsymbol{J} \tag{15}$$

$$\frac{1}{\sigma}\boldsymbol{J} = \boldsymbol{E} + \boldsymbol{v} \times \boldsymbol{B} \tag{16}$$

$$\frac{\partial \boldsymbol{B}}{\partial t} = -\nabla \times \boldsymbol{E} \tag{17}$$

Here, μ_{m} is the magnetic permeability and σ is the electrical conductivity of the fluid.

Combining Ampère's Law (15) and Ohm's Law (16), we get

$$\boldsymbol{E} = -\boldsymbol{v} \times \boldsymbol{B} + \frac{1}{\mu_{\mathrm{m}}\sigma}\nabla \times \boldsymbol{B} \tag{18}$$

and the Maxwell-Faraday Eq. (17) becomes

$$\frac{\partial \boldsymbol{B}}{\partial t} = \nabla \times (\boldsymbol{v} \times \boldsymbol{B}) - \nabla \times \left(\frac{1}{\mu_{\mathrm{m}}\sigma}\nabla \times \boldsymbol{B}\right) \tag{19}$$

Equation (19) then transforms as follows:

$$\frac{\partial \boldsymbol{B}}{\partial t} + (\boldsymbol{v} \cdot \nabla)\boldsymbol{B} = (\boldsymbol{B} \cdot \nabla)\boldsymbol{v} + \frac{1}{\mu_{\mathrm{m}}\sigma}\nabla^2 \boldsymbol{B} + \frac{1}{\sigma}(\nabla\sigma) \times \boldsymbol{E} + \frac{1}{\sigma}\nabla\sigma \times (\boldsymbol{v} \times \boldsymbol{B}). \tag{20}$$

In Fluent, the induction Eq. (20) is implemented for constant conductivity σ. The last two terms on the right-hand side of Eq. (20) are neglected. These terms are important

OSD
9, 2915–2950, 2012

in situations where one needs to account for variable conductivity, such as across the air-sea interface. However, since the work presented in this paper is concerned with the induced magnetic fields in the water only, we use the equation for constant conductivity provided within the Fluent software.

The magnetic field can generally be decomposed into the externally imposed field $\boldsymbol{B}_0$ and the induced field $\boldsymbol{b}$, which is due to fluid motion. Only the induced field needs to be solved and, in a conducting medium, the model solves the following equations:

$$\frac{\partial \boldsymbol{b}}{\partial t} + (\boldsymbol{v}\cdot\nabla)\boldsymbol{b} = ((\boldsymbol{B}_0+\boldsymbol{b})\cdot\nabla)\boldsymbol{v} + \frac{1}{\mu_\mathrm{m}\sigma}\nabla^2\boldsymbol{b} - (\boldsymbol{v}\cdot\nabla)\boldsymbol{B}_0 \tag{21}$$

$$\boldsymbol{J} = \frac{1}{\mu_\mathrm{m}}\nabla\times(\boldsymbol{B}_0+\boldsymbol{b}). \tag{22}$$

2.3 Radar imaging model

We combine the results from the CFD model with the radar imaging model M4S (Romeiser, 2008). The detailed description of the radar imaging model is beyond the scope of this paper and can be found in Romeiser et al. (1997) and Romeiser and Alpers (1997). The approach of combining results from CFD with a radar imaging model has previously been introduced by Fujimura et al. (2010). The combined use of results from a hydrodynamic model of the centerline ship wake with M4S has also been described and tested (Fujimura et al., 2012).

The surface velocity fields from the hydrodynamic model are used as input for the radar model. The settings for the radar imaging model are 9.65 GHz (X-band), HH polarization, 35° incidence angle, and 180° look direction. This corresponds to a look direction along the x-direction of the CFD model domains. We explored the use of different look directions in the M4S settings and found the choice did not significantly affect our results. Here, we ignore the effect of wind stress on the hydrodynamics, however, we set a wind speed of $4\,\mathrm{m\,s^{-1}}$ along x in the M4S model.

OSD
9, 2915–2950, 2012

2.4 CFD model setup and parameters

The model used a pressure-based solver with the Pressure-Implicit with Splitting of Operators (PISO) scheme for pressure-velocity coupling. For spatial discretization, the Pressure Staggering Option (PRESTO) scheme was used for pressure and 2nd order accuracy schemes for the momentum, energy and induction equations. The time-stepping scheme was set to 2nd order implicit. The material properties in the domain were specified as those of pure water or sea water (Table 1) using the Boussinesq model, which treats density as a constant value in all solved equations, except for the buoyancy term in the momentum equation. This model uses the linearized equation of state for density. The operating pressure was set to atmospheric pressure 101 325 Pa. Background stratification for the ship wake model changed linearly from $T = 296.65$ K to $T = 297.15$ K in the depth range from −6 m to −1 m and from $T = 294.15$ K to $T = 297.15$ K in the depth range from −16 m to −6 m for the plume model. The unstratified ship wake model had a constant initial temperature of 293.15 K. The stratification for the internal wave model was chosen to resemble a typical January stratification on the South East Florida shelf and ranged from $T = 283.15$ K to $T = 293.15$ K changing linearly in the depth range from −200 m to −100 m. The operating temperature was set to 297.15 K for the ship wake (293.15 K for the unstratified case), 293.15 K for the plume simulations, and 288.15 K for the internal wave simulation. The grid dimensions and time steps for ship wake, low density plume and internal wave simulations are given in Table 2.

For the simulations using the electromagnetic model, the external magnetic field was set to that of the Earth's magnetic field close to our location in South Florida, with the components $B_0\_x = -2.7e-06$ Tesla, $B_0\_y = 2.52e-05$ Tesla and $B_0\_z = -3.7e-05$ Tesla.

The boundary conditions for the hydrodynamic model, for both ship wake and near-surface low density plume, were set to periodic along the wake and in the direction of the buoyancy current propagation and to zero shear stress (equivalent of free-slip

OSD
9, 2915–2950, 2012

condition) and no heat flux at all other sides. The boundary conditions for the electromagnetic model of the ship wake were conducting at the top and bottom, and insulating at the non-periodic sides. The same boundary conditions were applied for the low density plume, top and bottom conducting, the non-periodic sides insulating.

The boundary conditions for the internal wave simulations for the hydrodynamic model were a zero shear stress wall at the eastern boundary and outflow at the western boundary (along the direction of wave propagation), as well as a zero shear stress wall at the top and a no-slip bottom. The north-south sides (across the direction of wave propagation), were set to velocity inlet conditions with the temperature set to a prescribed initial temperature profile. This was done to account for any mass lost at the outflow boundary. The inflow coming through these sides is negligible in our simulations. All other boundaries were set to zero heat flux. The boundary conditions on the electromagnetic model were set to conducting at the bottom and top, to zero flux at the velocity inlets and insulating at the eastern wall.

The simulations were run in parallel on 8 processors on Dell Precision T7400 work stations with two Quad-Core Intel Xeon processors and 64-bit Windows operating system.

3 Results

3.1 Ship wakes

Details of the ship wake model have previously been described by Fujimura et al. (2012). This model of the far wake of a ship is initialized with velocity fields from a near wake simulation of flow around a surface ship hull with modeled propeller wakes (Rhee and Kim, 2008). The periodic boundary conditions along the wake allow the investigation of the time evolution of the wake, simulating a decaying wake after the passage of a vessel.

OSD
9, 2915–2950, 2012

In this paper, we investigate the effect of a thermal stratification in the oceanic near-surface layer on the wake hydrodynamics and surface signature. We found that cold subsurface water may be brought to the surface through the circulation in the ship wake (Fig. 1). This sea surface signature in the temperature field may be detected by infrared sensors of the sea surface. This result is consistent with in-situ observations of a ship wake signature in the temperature field in the Straits of Florida presented in a companion paper (Soloviev et al., 2012). Stratification also appears to have an effect on the surface spreading of the wake, as well as on subsurface small-scale turbulent fluctuations (Fig. 2). In the presence of a stratified ambient, the wake circulation in the shallower layers of the water column appears more compact, with less of a downward extent. The sea surface signature of the wake can be seen in the velocity field as well as in the radar backscatter intensity map, which is a proxy for a SAR image (Fig. 3). In the case of a near-surface thermal stratification, the wake surface signature appears slightly wider and more pronounced than is the case without stratification (Fig. 4).

Combining the ship wake hydrodynamic model with the electromagnetic model within the CFD framework, allows the investigation of the ship wake signature in the ocean magnetic field. The induced field reaches values of the order of 10^{-11} Tesla, which is on the lower boundary of what is possible to detect with modern magnetometers (Fig. 5). However, the idealized and scaled ship model for our ship wake model is relatively small ($\sim$ 6 m length) and we expect to see a larger signal for a larger vessel with more intense wake circulation. Furthermore, in our simulations, we use as external field strength the value for the Earth's magnetic field close to our location in South Florida. At higher latitudes, the induced magnetic field is expected to be larger due to an increase in the strength of the geomagnetic field near the poles.

Note that our results suggest that in an oceanic setting, the ship's wake may be detected in the magnetic field for tens of minutes after the ship has passed through the observational domain. Combining data from magnetometers with SAR imagery of ship wakes may add a valuable new dimension to ship surveillance and detection.

OSD
9, 2915–2950, 2012

3.2 Near-surface buoyancy currents

The setup and initial conditions for the simulation of near-surface buoyancy driven currents associated with a low density plume are shown in Fig. 6. The model is initialized with a temperature anomaly in the near-surface layer, simulating a rain-formed plume. This parcel of low density water then propagates in the upper layer of the water column as a buoyancy-driven current. The flow exhibits features of a classic gravity current, including the gravity current head and a tail region, where Kelvin-Helmholtz overturns are apparent and contribute to mixing (Fig. 7). As the near-surface low density plume propagates into the stratified environment, internal waves are excited in the thermocline. This then leads to a resonant interaction between the internal waves and the near-surface current, which results in a fragmentation of the low density plume. The fragmentation becomes apparent as a banding pattern on the sea surface in the velocity field (Fig. 8). This pattern of alternating bands can also be seen in the sea surface signature in the simulated radar image (Fig. 9). Under certain conditions, river plumes are known to generate large amplitude internal waves at their leading edge (Nash and Moum, 2005). These can exhibit a signature on the sea surface in SAR similar to that seen in our results.

Our results are consistent with observations of freshwater plumes in the Western Equatorial Pacific (Soloviev and Lukas, 2006). Following Soloviev and Lukas (2006), to generate internal waves the Froude number Fr should satisfy

$$Fr = \frac{\sqrt{g' h}}{NH} < {}^{1}/_{\pi} \tag{23}$$

and

$$\frac{h}{H} < 0.2. \tag{24}$$

OSD
9, 2915–2950, 2012

Here, $g' = g\frac{\Delta\rho}{\rho_0}$ is the reduced gravity, $N^2 = -\frac{g}{\rho_0}\frac{\partial\rho}{\partial z}$ is the Brunt-Väisällä frequency, h is the depth of the gravity current, and H is the total water depth. Conditions (21) and (22) are satisfied in the numerical experiments presented here.

When investigating the magnetic signature associated with the low density plume, it is found that the magnetic signal follows the propagating density current front and reaches magnitudes of the order of 10^{-10} Tesla (Fig. 10). A propagating rain-formed or river plume is therefore expected to produce a measurable magnetic signature, especially for cases with large freshwater inflow and strong density contrast.

3.3 Internal waves

The model setup for the simulation of an internal wave soliton and the ambient stratification (Fig. 11) were chosen to resemble the environment observed in the Straits of Florida by Soloviev et al. (2012) on 16 January 2011. The wave is generated via a density anomaly that initially propagates as gravity current but after reflection from the wall boundary develops an internal wave in the thermocline resembling a soliton (Fig. 12). This internal wave produces a strong signal in the induced magnetic field, reaching tens of nT at the leading edge of the wave (Fig. 13).

To calculate the commonly reported total magnetic field, we computed the magnetic field from the vector components and removed the Earth field bias to generate the residual field displayed in Fig. 14. The simulated internal wave generates a total magnetic field signature in the 1–1.5 nT range, which is well within the range detectable by modern magnetometers. Note that the internal wave signature can be observed in both the velocity field and the magnetic field.

Simulating the placement of a magnetometer at 2 m off the bottom in an L-shaped array allows the investigation of time series data of the signal in the total magnetic field (Fig. 15). The variation in the total magnetic field in the direction of wave propagation shows the wave pattern and a phase shift as the signal passes the measurement points. There is little along-shelf variation due to the 2-D nature of the simulated

OSD
9, 2915–2950, 2012

internal wave, which is propagating onto the shelf (east to west) in this simulation. This approach of simulating sensor placement can be helpful to determine the ideal configuration of magnetometers and hydrographic instruments for ocean magnetic observatories.

Finally, combining the horizontal velocities at the sea surface from the numerical model with a radar imaging model, the internal wave signature can also be observed in the radar backscatter intensity map of the sea surface (Fig. 16). The internal wave signature is thus clearly seen in the velocity field, the magnetic field, as well as the simulated radar image. This suggests that data from magnetometers, oceanographic instruments and SAR satellites can complement each other to provide a comprehensive picture of dynamic processes in the upper ocean.

4 Summary and discussion

The approach used in this work, of combining a three-dimensional CFD model, including an electromagnetic module, with a radar imaging model, can be useful for the simulation of fine-scale features on the sea surface and their interpretation in high-resolution SAR images. We were able to reproduce the sea surface signatures of centerline wakes of ships, low density plumes and internal waves in SAR. The results are qualitatively consistent with available SAR images of ship wakes, freshwater plumes and internal waves. In the case of a thermal stratification in the oceanic near-surface layer, colder subsurface water may be brought to the surface through the circulation in the ship wake and the stratification affects the signature of the wake at the surface by limiting the downward spreading of the wake. The model of a low density near-surface plume revealed that, as the plume propagates into a stratified environment, the interaction with the ambient stratification can lead to internal waves and a fragmentation of the plume. This fragmentation can be seen as alternating bands in the sea surface signature in simulated radar images. Internal waves can produce prominent sea surface signatures in SAR and can also lead to a signal in the measured electromagnetic

OSD
9, 2915–2950, 2012

field in the ocean. We reproduced the electromagnetic signatures of internal waves, low density plumes and ship wakes in the total magnetic field.

The results presented in this work provide a link between SAR signatures of transient ocean dynamics and magnetic field fluctuations in the ocean. This suggests that combining SAR imagery with data from magnetometers may offer a valuable new prospect in maritime sensing.

Acknowledgements. This work was supported by the project "Hydrodynamics and Remote Sensing of Far Wakes of Ships" at NSUOC and by ONR Award N00014-10-1-0938 "Characterization of Impact of Oceanographic Features on the Electromagnetic Fields in Coastal Waters". We are grateful to Richard Dodge (NSUOC) and Will Avera (NRLSSC) for helpful discussions of the problem. We thank Mikhail Gilman for help with programming user-defined functions for CFD.

References

Alpers, W.: Theory of radar imaging of internal waves, Nature, 314, 245–247, 1985.

Alpers, W., Brandt, P., and Rubino, A.: Internal waves generated in the Straits of Gibraltar and Messina: Observations from space, in: Remote Sensing of the European Seas, Springer, Heidelberg, 319–330, 2008.

Beal, H. T. and Weaver, J. T.: Calculations of Magnetic Variations Induced by Internal Ocean Waves, J. Geophys. Res., 75, 6846–6852, 1970.

Brusch, S., Lehner, S., and Reppucci, A.: SAR Derived Wind Fields of Mesoscale Cyclones, Geoscience and Remote Sensing Symposium, IGARSS 2008 IEEE International, 2, 489–492, 2008.

Crews, A. and Futterman, J.: Geomagnetic Micropulsations Due to the Motion of Ocean Waves, J. Geophys. Res., 67, 299–306, 1962.

Fujimura, A., Soloviev, A., and Kudryavtsev, V.: Numerical Simulation of the Wind-Stress Effect on SAR Imagery of Far Wakes of Ships, IEEE Geosci. Remote Sens. Lett., 7, 646–649, 2010.

OSD

9, 2915–2950, 2012

Fujimura, A., Matt, S., Soloviev, A., Maingot, C., and Rhee, S. H.: The impact of thermal stratification and wind stress on sea surface features in SAR imagery, IEEE International Geoscience & Remote Sensing Symposium (IGARSS) Proceedings, 2037–2040, 2011.

Fujimura, A., Soloviev, A., Rhee, S. H., and Romeiser, R.: Coupled Model Simulation of Wind Stress Effect on Far Wakes of Ships in SAR Images, submitted, 2012.

Gade, M., Alpers, W., Hühnerfuss, H., Masuko, H., and Kobayashi, T.: Imaging of biogenic and anthropogenic ocean surface films by the multifrequency/multipolarization SIR-C/X-SAR, J. Geophys. Res., 103, 18851–18866, 1998.

Hinze, J. O.: Turbulence, McGraw-Hill, New York, 1975.

Horstmann, J. Koch, W., Lehner, S., and Tonboe R.: Wind Retrieval over the Ocean using Synthetic Aperture Radar with C-band HH Polarization, IEEE Trans. Geosci. Remote, 38, 2122–2131, 2000.

Hsu, M.-K., Liu, A. K., and Liu, C.: A study of internal waves in the China Seas and Yellow Sea using SAR, Cont. Shelf Res., 20, 389–410, 2000.

Hühnerfuss, H., Walter, W., Lange, P. A., and Alpers, W.: Attenuation of wind waves by monomolecular sea slicks and the Marangoni effect, J. Geophys. Res., 92, 3961–3963, 1987.

Matt, S., Fujimura, A., Soloviev, A., and Rhee, S. H.: Modification of Turbulence at the Air-Sea Interface Due to the Presence of Surfactants and Implications for Gas Exchange. Part II: Numerical Simulations, in: GAS TRANSFER AT WATER SURFACES 2010, Kyoto University Press, 299–312, 2011.

Milgram, J. H., Peltzer, R. D., and Griffin, O. M.: Suppression of short sea waves in ship wakes: measurements and observations, J. Geophys. Res., 98, 7103–7114, 1993a.

Milgram, J. H., Skop, R. A., Peltzer, R. D., and Griffin, O. M.: Modeling short sea wave energy distribution in the far wakes of ships, J. Geophys. Res., 98, 7115–7124, 1993b.

Nash, J. D. and Moum, J. N.: River plumes as a source of large-amplitude internal waves in the coastal ocean, Nature, 437, 400–403, 2005.

Reed, A. M. and Milgram, J. H.: Ship wakes and their radar images, Annu. Rev. Fluid Mech., 34, 469–502, 2002.

Romeiser, R., Alpers, W., and Wismann, V.: An improved composite surface model for the radar backscattering cross section of the ocean surface, 1. Theory of the model and optimization/validation by scatterometer data, J. Geophys. Res., 102, 25237–25250, 1997.

OSD
9, 2915–2950, 2012

Romeiser, R. and Alpers, W.: An improved composite surface model for the radar backscattering cross section of the ocean surface, 2. Model response to surface roughness variations and the radar imaging of underwater bottom topography, J. Geophys. Res., 102, 25251–25267, 1997.
Romeiser, R., Ufermann, S., and Kern, S.: Remote sensing of oceanic current features by synthetic aperture radar - achievements and perspectives, Annals of Telecommunications, 56, 661–671, 2001.
Romeiser, R., Suchandt, S., Runge, H., Steinbrecher, U., and Grünler, S.: First analysis of TerraSAR-X along-track InSAR-derived current fields, IEEE Trans. Geosci. Remote, 48, 820–829, 2010.
Romeiser, R.: M4S 3.2.0 User's Manual, University of Hamburg, Hamburg, Germany, 2008.
Rhee, S. H. and Kim, H.: A suggestion of gap flow control devices for the suppression of rudder cavitation, J. Mar. Sci. Technol., 13, 356–370, 2008.
Smagorinsky, J.: General Circulation Experiments with the Primitive Equations. I. The Basic Experiment, Month. Weather Rev., 91, 99–164, 1963.
Soloviev, A. and Lukas, R.: The Near-Surface Layer of the Ocean: Structure, Dynamics, and Applications, Springer, New York, 572 pp., 2006.
Soloviev, A., Gilman, M., Moore, K., Young, K., and Graber, H.: Hydrodynamics and Remote Sensing of Far Wakes of Ships, *SEASAR 2008* – The 2nd Int. Workshop on Advances in SAR Oceanography, Frascati, Italy, 21–25 January 2008.
Soloviev, A., Gilman, M., Young, K., Brusch, S., and Lehner, S.: Sonar measurements in ship wakes simultaneous with TerraSAR-X overpasses, IEEE T. Geosci. Remote, 48, 841–851, 2010.
Soloviev, A. V., Matt, S., Gilman, M., Hühnerfuss, H., Haus, B., Jeong, D., Savelyev, I., and Donelan, M.: Modification of Turbulence at the Air-Sea Interface Due to the Presence of Surfactants and Implications for Gas Exchange. Part I: Laboratory Experiment, in: GAS TRANSFER AT WATER SURFACES 2010, Kyoto University Press, 285–298, 2011.
Soloviev, A., Maingot, C., Matt, S., Dodge, D., Lehner, S., Velotto, D., Brusch, S., Perrie, W., and Hochberg, E.: Fine-scale features on the sea surface in SAR satellite imagery – Part 1: Simultaneous in-situ measurements, Ocean Sci. Discuss., 9, 2885–2914, doi:10.5194/osd-9-2885-2012, 2012.

OSD
9, 2915–2950, 2012

Table 1. Material properties.

Experiment	Molecular dynamic viscosity μ kg m^{-1} s^{-1}	Thermal conductivity κ W m^{-1} K^{-1}	Magnetic permeability μ_m H m^{-1}	Electrical conductivity σ S m^{-1}	Specific heat c_p J kg^{-1}K^{-1}	Density ρ kg m^{-3}
Ship wake, without stratification	1.08×10^{-3}	0.596	–	–	3993	998.2
Ship wake, with stratification	1.08×10^{-3}	0.596	1.257×10^{-6}	4.788	3993	1024.75
Plume	1.08×10^{-3}	0.596	1.257×10^{-6}	4.788	3993	1024.75
Internal Wave	1.08×10^{-3}	0.596	1.257×10^{-6}	4.788	3993	1024.75

OSD
9, 2915–2950, 2012

Table 2. Grid dimensions and time steps for ship wake, low density plume and internal wave simulations. The vertical resolution for the ship wake and plume model is highest near the top of the domain and decreases towards the bottom. For the internal wave model, the highest vertical resolution is in the thermocline.

Experiment	Length x, m	Width y, m	Height z, m	Δx, m	Δy, m	Δz, m	Time step Δt, s
Ship wake	50	50	10	0.5	0.2	0.001 (top cell)	0.025
Plume	500	40	40	0.5	1	0.01 (top cell)	0.5
Internal wave	2000	1000	250	10	10	1–2	5

OSD
9, 2915–2950, 2012

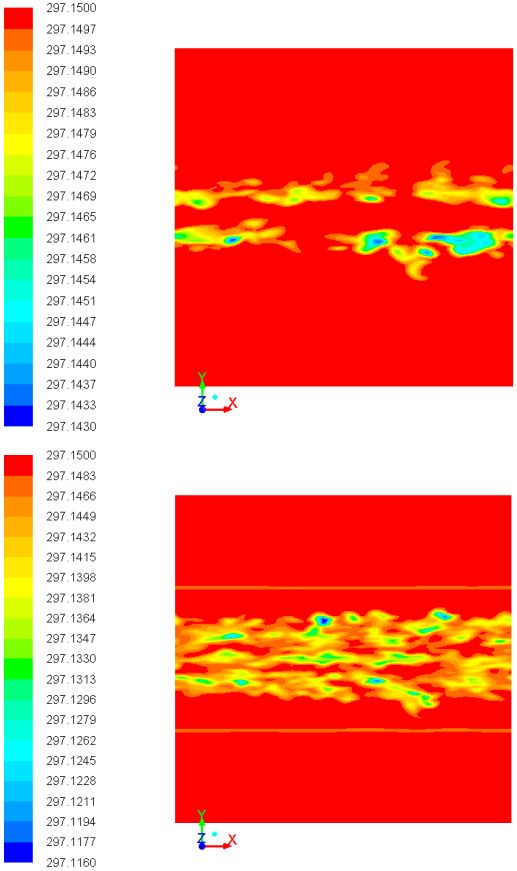

Fig. 1. Top view of temperature field (in Kelvin, at time t = 575 s) for ship wake model in the presence of an ambient stratification illustrates the upwelling of colder subsurface water by the circulation in the ship wake. Top: at depth 5 mm; bottom: at depth 0.5 m.

OSD
9, 2915–2950, 2012

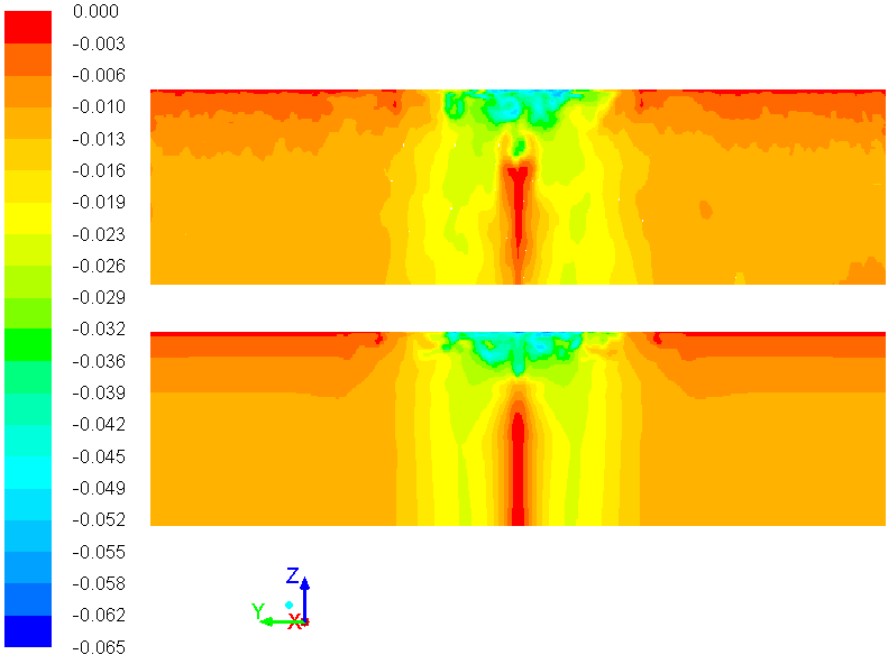

Fig. 2. Side view of x-velocity (in $m\,s^{-1}$, at time $t = 575$ s) for ship wake model without (top) and with (bottom) ambient stratification. The stratification appears to affect the spreading of the wake at the surface and to suppress background turbulent fluctuations in the model.

OSD
9, 2915–2950, 2012

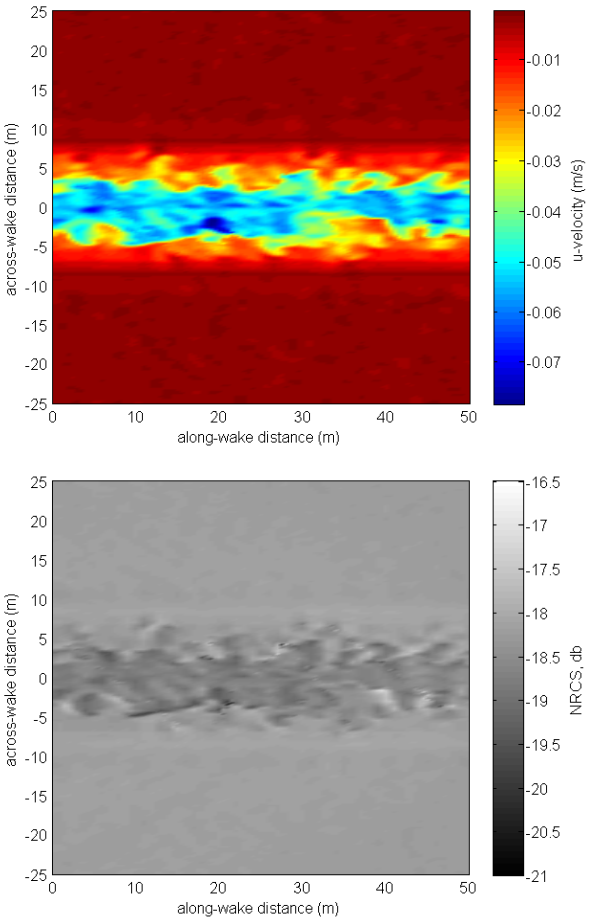

Fig. 3. Ship wake signature at the surface in the velocity field (top, in m s^{-1}) and radar backscatter intensity map (bottom; as normalized radar cross section (NCRS), db values here should be taken as relative) for the case without ambient stratification. Taken at time t = 575 s.

OSD
9, 2915–2950, 2012

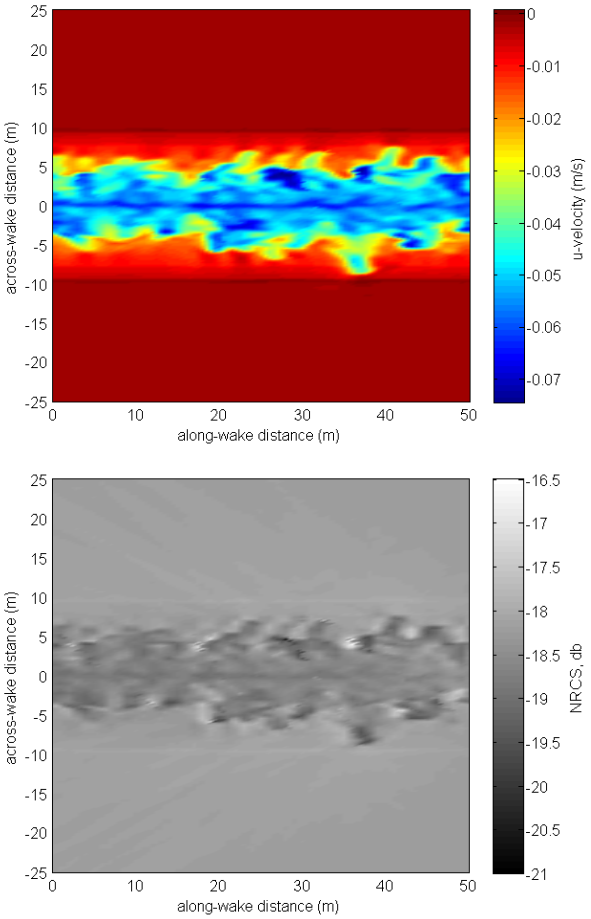

Fig. 4. Ship wake signature at the surface in the velocity field (top, in m s^{-1}) and radar backscatter intensity map (bottom, db values here should be taken as relative) for the case with ambient stratification. Taken at time t = 575 s.

OSD
9, 2915–2950, 2012

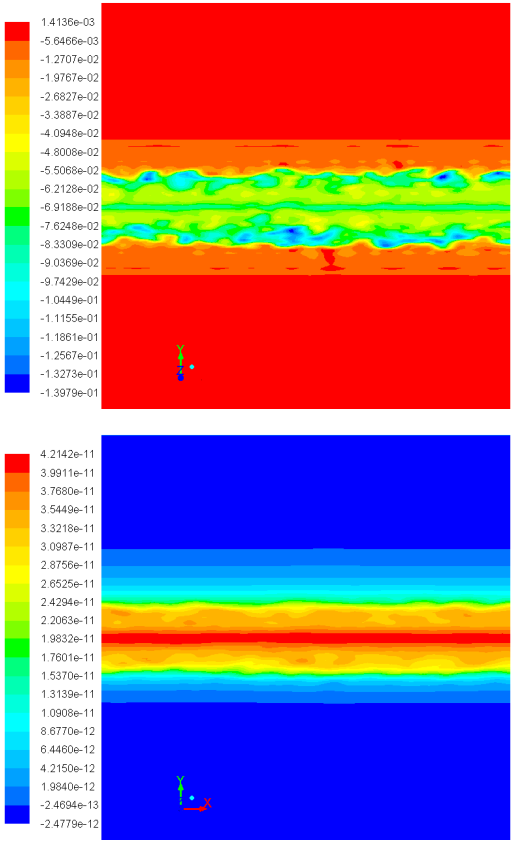

Fig. 5. Top view of ship wake signature in the velocity field (top: x-velocity at the surface in $m\,s^{-1}$) and induced magnetic field (bottom: Bx at the surface in Tesla) for the case with ambient stratification. Taken at time t = 200 s.

OSD
9, 2915–2950, 2012

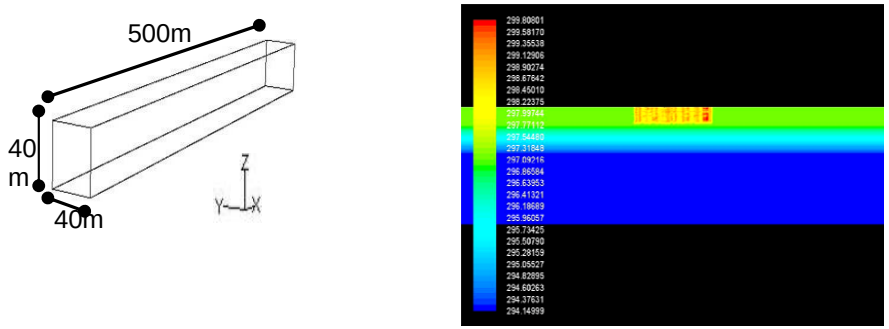

Fig. 6. Model domain (left) and side view of initial condition in the temperature field (right; at t = 0 s, in Kelvin) for the low density plume simulation. Model horizontal resolution is 0.5 m in x by 1 m in y and vertical resolution is 1 cm at the top (with decreasing vertical resolution towards the bottom).

OSD
9, 2915–2950, 2012

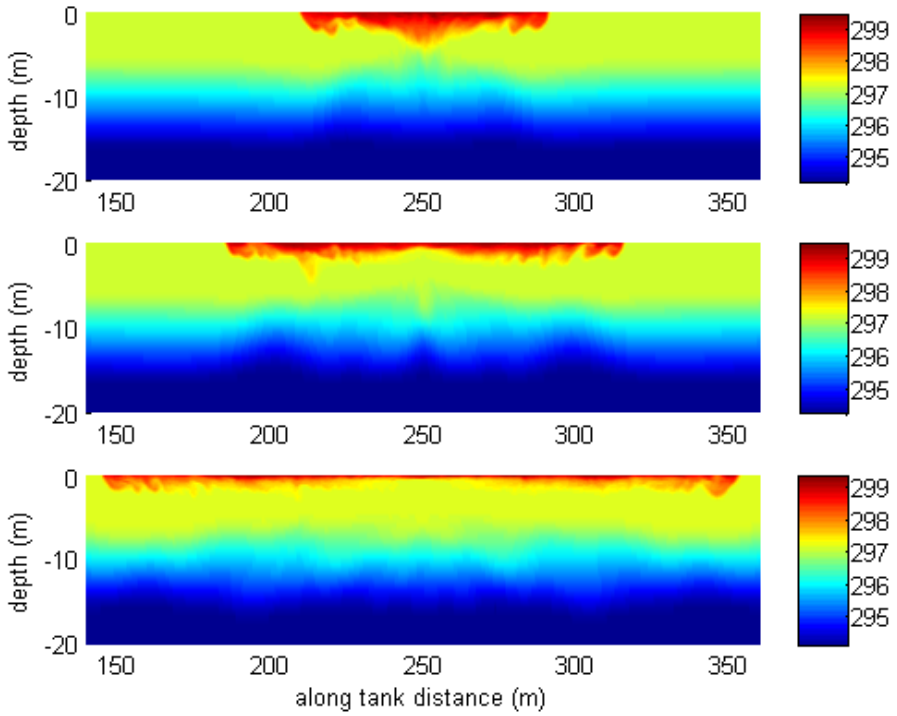

Fig. 7. Close-up of a side view of temperature (in Kelvin) illustrates the propagation of the low density plume in the near-surface layer and the internal waves generated in the thermocline. Time evolution is from top to bottom. Top: after time 300 s, middle: after 1500 s, bottom: after 2000 s.

OSD
9, 2915–2950, 2012

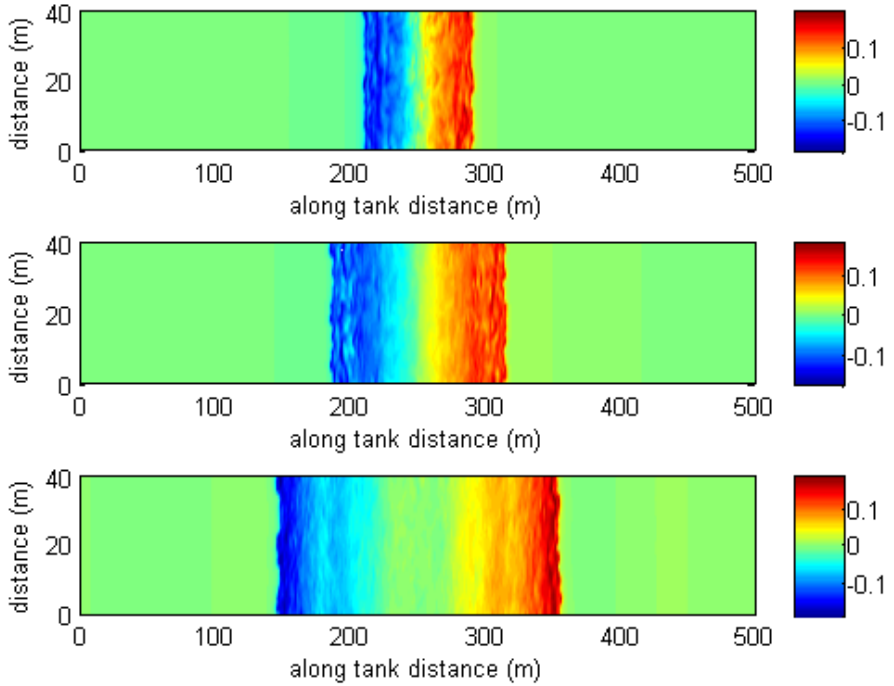

Fig. 8. Top view of the along-tank (x-) velocity (in $m\,s^{-1}$) showing the evolution of the density current front and the fragmentation (surface "lines") that occurs due to the interaction of the density current with the ambient stratification. Top: after time 300 s, middle: after 1500 s, bottom: after 2000 s.

OSD
9, 2915–2950, 2012

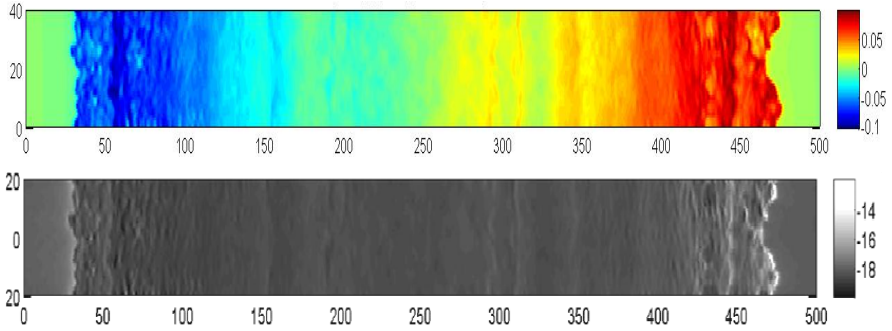

Fig. 9. Surface signature of low density plume in the velocity field (top, in $m\,s^{-1}$) and radar backscatter intensity map (bottom; NRCS, db-values here should be taken as relative). x-axis shows along-tank distance, y-axis is across-tank distance (in m). Taken at time t = 2850 s.

OSD
9, 2915–2950, 2012

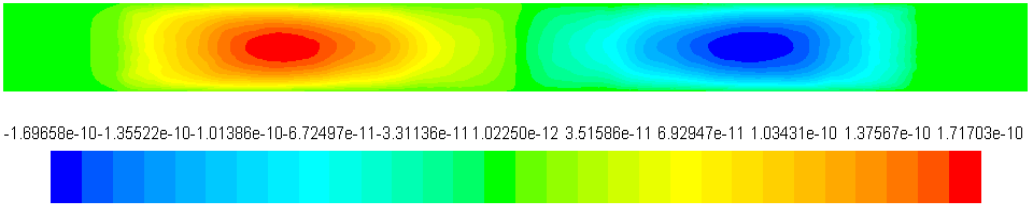

Fig. 10. Surface signature of low density plume in the induced magnetic field (Bx, in Tesla) for the same projection as in Fig. 9, at time t = 2350 s.

OSD
9, 2915–2950, 2012

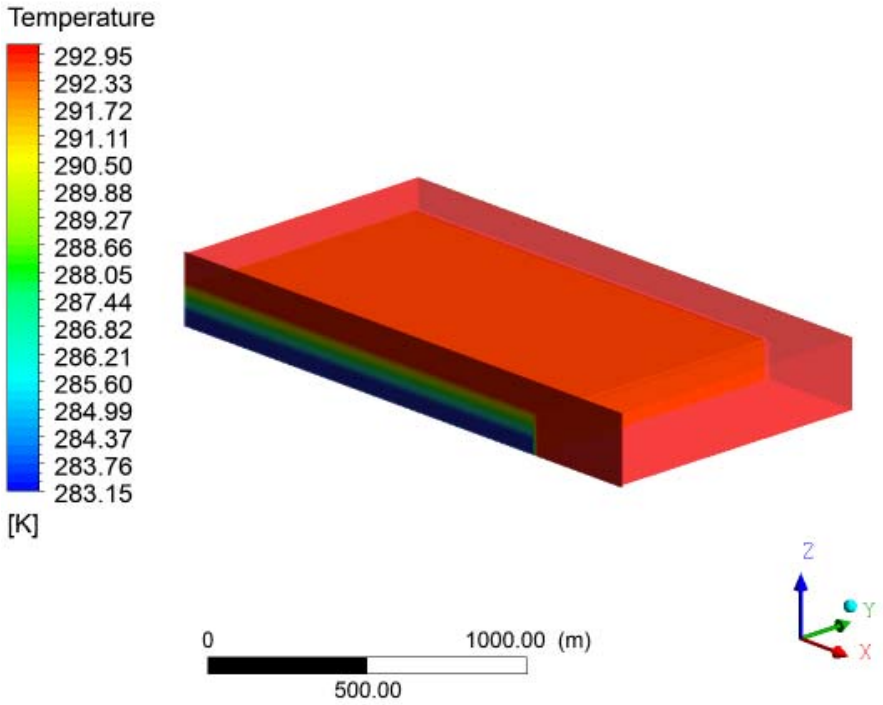

Fig. 11. Initial condition for internal wave simulation shown in the model temperature field (in Kelvin). Domain length (x) is 2 km ; domain width (y) is 1 km; domain depth (z) is 250 m. Model horizontal resolution is 10 m and vertical resolution 2 m, with increased vertical resolution in the thermocline.

OSD
9, 2915–2950, 2012

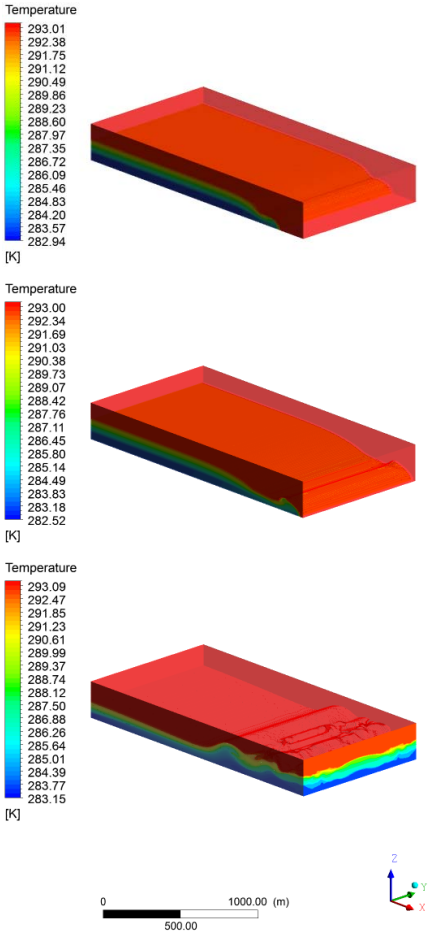

Fig. 12. Evolution of internal wave simulation in the model temperature field (in Kelvin). Time evolution is from top to bottom. Top: after time 200 s, middle: after 400 s, bottom: after 1800 s.

OSD
9, 2915–2950, 2012

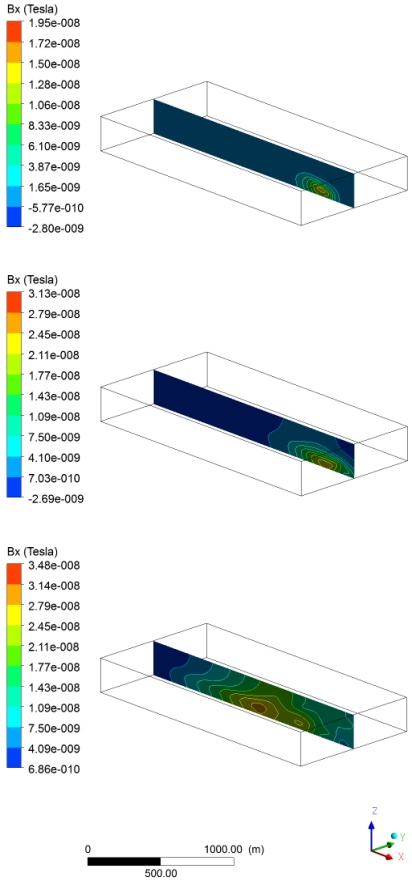

Fig. 13. Evolution of induced magnetic field component Bx for the internal wave simulation shown in Fig. 12. Time evolution is from top to bottom. Top: after time 200 s, middle: after 400 s, bottom: after 1800 s.

OSD
9, 2915–2950, 2012

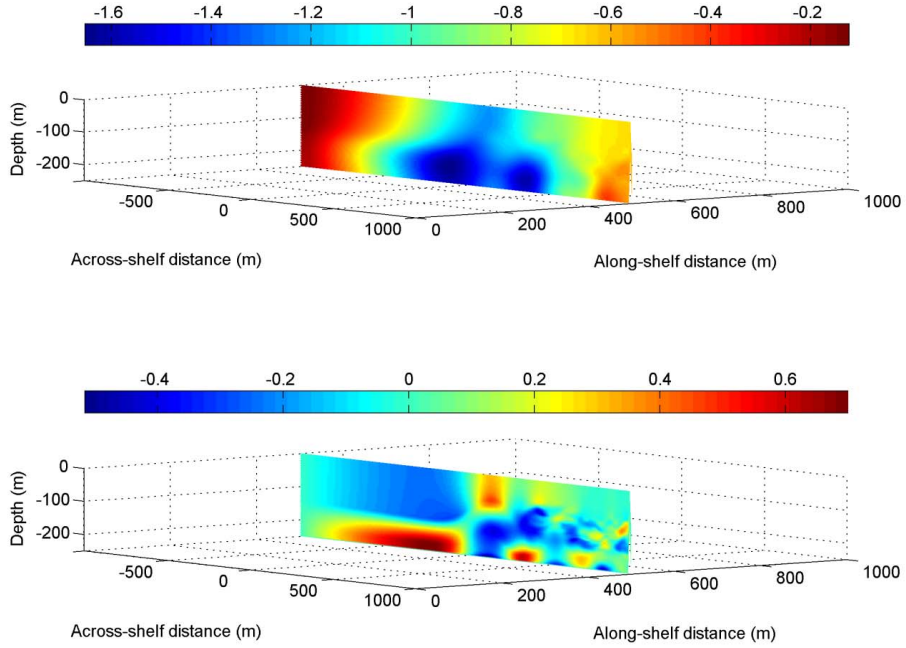

Fig. 14. Top: the total magnetic field is computed from the vector components and the Earth field bias is removed to generate the displayed residual field (in nT). Bottom: velocity component in direction of wave propagation (in $m\,s^{-1}$). Both for time t = 2000 s.

OSD
9, 2915–2950, 2012

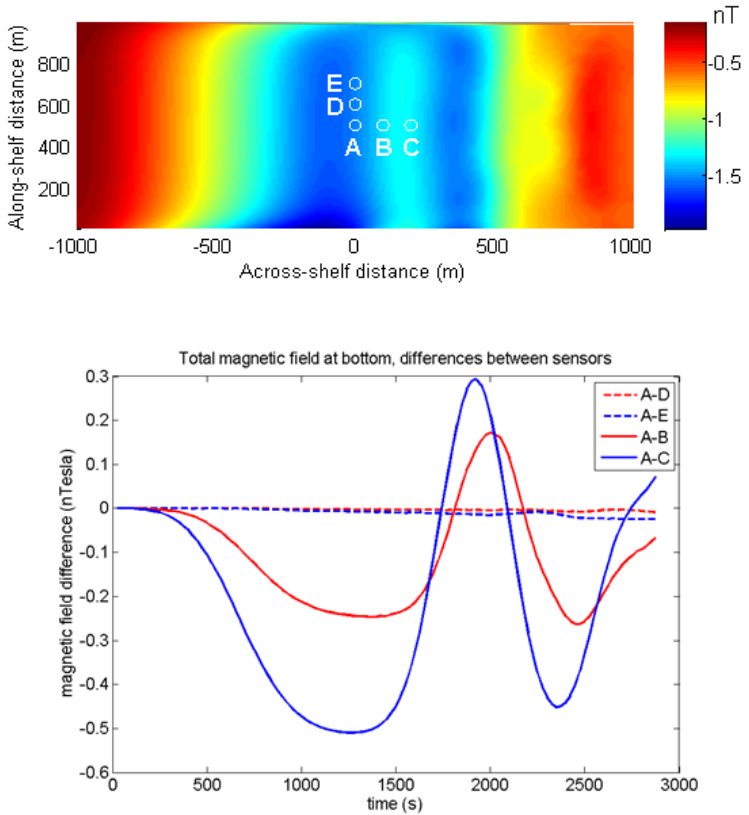

Fig. 15. Simulated sensors placement in the model is shown in the total magnetic field at 2 m off the bottom at time $t = 2000$ s (top). Data points are taken from an L-shaped array in the model to compare time series of the signal in the total magnetic field (bottom). The differences between sensors are shown.

OSD
9, 2915–2950, 2012

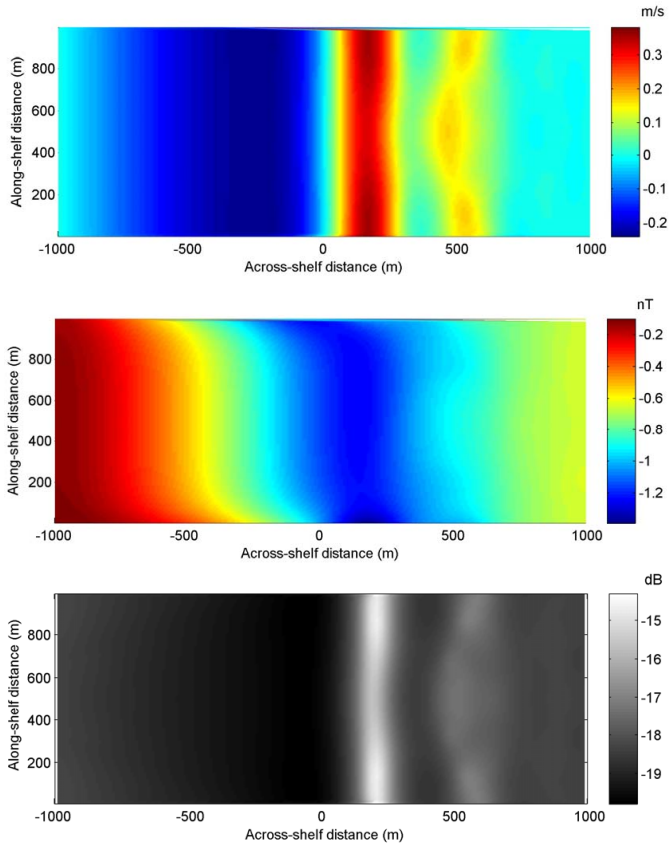

Fig. 16. Internal wave signature in velocity field (top), in total magnetic field (middle), both at 1cm depth, and radar backscatter intensity map (bottom; NRCS, db-values here should be taken as relative). Taken at time t = 2000 s.

OSD
9, 2915–2950, 2012